eng

MDPI

Article

Experimental and Numerical Investigation of Oil Removal in Oil-Contaminated Wastewater Using Membrane Treatment

Ali Shahin [1] and Rached Ben-Mansour [1,2,*]

[1] Mechanical Engineering Department, King Fahd University of Petroleum and Minerals (KFUPM), Dhahran 31261, Saudi Arabia; g202303690@kfupm.edu.sa
[2] IRC for Sustainable Energy Systems, King Fahd University of Petroleum and Minerals (KFUPM), Dhahran 31261, Saudi Arabia
* Correspondence: rmansour@kfupm.edu.sa

Abstract

The oil and gas industry is increasingly challenged by the global transition toward renewable energy systems aimed at reducing carbon emissions. Nevertheless, opportunities remain to mitigate the environmental impacts associated with ongoing oil and gas operations. One of the major environmental challenges in this sector is the extensive use and treatment of water. Membrane-based separation has emerged as an effective technology for oil–water separation due to its ability to overcome limitations associated with conventional treatment methods. This study aims to build a CFD model to investigates the influence of operational hydrodynamic conditions on membrane separation, including transmembrane pressure 202, 101, 50, 10 kPa, crossflow velocity 0.08 m/s, 0.116 m/s, 0.33 m/s, 0.66 m/s, and oil droplet diameter 1, 5, 10, 50, 100 μm, on membrane performance in addition to different oil concentrations 1%, 2%, 4%, 8% using Eulerian-Eulerian multiphase model. This is done by experimentally extracting the membrane water resistance, which is found to be 6.46×10^{10} (1/m) and using it as an input to the numerical model. The results indicate that permeate flux is primarily governed by transmembrane pressure, in agreement with Darcy's law, while fouling development along the membrane length is mainly influenced by crossflow velocity and oil droplet size. Where it was found that for large droplets 100 μm and 50 μm the buoyancy forces were large enough to lift the oil droplets away from the membrane at velocities 0.08, 0.16 and 0.33 m/s while smaller droplets remained at the membrane surface In addition, backward diffusion, which has been emphasized in previous studies, was found to play a comparatively minor role in the present numerical analysis.

Keywords: wastewater; membrane; multiphase; oil; treatment; CFD

Check for updates

Academic Editor: Diego Luna

Received: 5 February 2026
Revised: 25 March 2026
Accepted: 31 March 2026
Published: 7 April 2026

Copyright: © 2026 by the authors. Licensee MDPI, Basel, Switzerland. This article is an open access article distributed under the terms and conditions of the Creative Commons Attribution (CC BY) license.

1. Introduction

The oil and gas sector is increasingly perceived as a declining industry, driven by the global transition toward renewable and sustainable energy alternatives [1]. Consequently, numerous corporations face escalating pressure to mitigate their carbon footprints in compliance with tightening regulatory frameworks [2]. Simultaneously, a primary technical hurdle for power grids with high renewable penetration is the inherent variability on diurnal, seasonal, and annual scales [3]. Given these systemic constraints and the existing infrastructure, major energy forecasts suggest that oil and natural gas will remain indispensable in the short to medium term, despite the rapid expansion of renewables [4]. However, this necessity does not preclude the implementation of field-level strategies designed to

minimize the environmental impact of hydrocarbon extraction. A prominent challenge currently confronting the industry is the intensive water consumption associated with the recovery of oil and gas from subsurface reservoirs.

Within the petroleum industry, the presence of water in the hydrocarbon stream is considered highly undesirable. This aqueous component originates either from naturally occurring sources, such as water trapped within or adjacent to hydrocarbon-bearing zones, or from secondary recovery methods where water is injected into wells to facilitate the migration of oil and gas to the surface [5]. Technically, the naturally occurring fraction is categorized as "connate water" or "formation water" [5]. In general, the water used or extracted with oil and gases from the wells, or the water being used in the oil and gas industry at any stage, is called produced water (PW) [6]. In 2018, the total produced water globally was 6855.3 million m^3, with the USA, Russia, and Saudi Arabia accounting for 3338.7 (48.7%), 1588.1 (23.17%), and 1307.6 (19.07%), respectively, in million m^3 and percentage [7]. Figure 1 illustrates the comparative volumes of PW across these three leading nations.

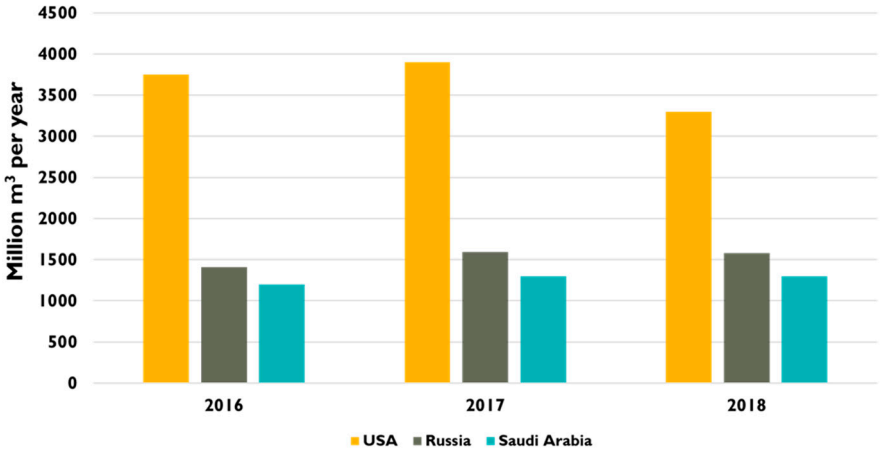

Figure 1. Total produced water volume for the top three countries in the world [3].

According to ARAMCO's annual reports from 2018 to 2024 [8], the frequency of oil spills has fluctuated between 6 and 15 incidents per year. Furthermore, significant volumes of hydrocarbons were discharged into marine environments during these years.

Designing an effective produced water (PW) treatment process within the oil and gas industry requires a comprehensive strategy based on the specific composition and concentration of contaminants, as well as the required purity standards for the final effluent. These treatment methodologies are generally categorized either by their operational stage, such as pretreatment, primary, secondary, and tertiary levels, or by their underlying mechanism, including physical, chemical, biological, thermal, or membrane-based processes. Various combinations of these techniques are frequently integrated to satisfy environmental regulations and operational targets.

Membrane technology is increasingly regarded as a favorable alternative in the petrochemical sector. This preference stems from its ability to address the shortcomings of conventional methods, such as the reliance on hazardous chemical reagents, the generation of secondary byproducts, and the necessity for complex infrastructure and equipment [9]. It is considered a promising technology for the 21st century [10].

Membranes are thin films of either inorganic or organic material used to separate fluid from the undesired components that flow with it [11]. They are broadly classified into two primary categories based on their driving force: pressure-driven or thermally driven systems. Thermally driven membranes, commonly referred to as membrane distilla-

tion (MD), have garnered significant academic and industrial interest. The fundamental principle involves a heated feed stream flowing across a hydrophobic membrane, where vapor from the hot side permeates the membrane and subsequently condenses on the cooler side. Operating typically at temperatures of 80 °C or lower, this method offers distinct advantages over conventional thermal distillation techniques [12]. However, a notable drawback of this approach is its current lack of energy efficiency and the logistical challenges associated with cooling system requirements. Research in this field remains ongoing to address these limitations.

Pressure-driven membranes function based on the differential concentration of materials across the medium, where the separation process is influenced by various factors such as surface characteristics and pore size. These parameters are critical in determining the selectivity of the membrane and the specific substances permitted to permeate the barrier. These systems are typically classified according to their nominal pore size into four primary categories, which include microfiltration (MF), ultrafiltration (UF), nanofiltration (NF), and reverse osmosis (RO) [13].

As the terminology implies, the fundamental driving force in pressure-driven membrane processes is the pressure differential across the medium, specifically the gradient between the feed and permeate sides. This parameter is formally defined as the transmembrane pressure (TMP). Consequently, the permeate flux traversing the membrane is directly proportional to the TMP and inversely related to the total resistance encountered by the solute flow. This relationship is characterized in the literature as the resistance-in-series model, which is primarily employed to describe microfiltration (MF) and ultrafiltration (UF) processes [14]. This model is conceptually derived from the resistance principles commonly found in heat transfer and electrical circuit theory. Within this framework, the total resistance is defined as the sum of various components, including the intrinsic membrane resistance observed with pure water. This model is conceptually derived from the resistance principles commonly found in heat transfer and electrical circuit theory. Within this framework, the total resistance is defined as the sum of various components, including the intrinsic membrane resistance observed with pure water (R_m), and additional resistances arising from phenomena such as fouling or concentration polarization ($R_{fouling}$).

To better understand and analyze the transport phenomena governing membrane performance, numerical modeling tools are often employed. In this context, Computational Fluid Dynamics (CFD) has emerged as a robust methodology for investigating fluid flow and mass transport within membrane systems. CFD is fundamentally established on the conservation laws of mass and linear momentum. The governing equations representing these principles are multivariable partial differential equations for which general analytical solutions do not exist. Consequently, these equations are transformed into solvable algebraic forms through discretization techniques. This process involves partitioning the computational domain into discrete elements and applying numerical schemes to obtain approximate solutions that satisfy the prescribed initial and boundary conditions. A comparative analysis of various discretization schemes utilized in CFD models is provided in [15].

The pioneering computational research on porous walls was conducted in 1953 by Berman [16], who investigated the hydrodynamic properties within a rectangular channel under the assumptions of laminar, steady-state, and incompressible flow. Subsequent studies have endeavored to accurately simulate flow exiting porous boundaries for both flat-sheet and cylindrical configurations. Further experimental investigations have assessed membrane separation performance through droplet-size analysis and the application of diverse fluid materials [17]. While some researchers have focused on varying operating pressures and modes of operation [18], others have explored the use of specialized materials, such as ceramic membranes with distinct pore sizes [19].

Additionally, the influences of concentration polarization (CP) and cake layer formation on rejection efficiency have been widely studied [20]. Although several papers have provided numerical modeling for these phenomena, the specific effects of pore blocking were frequently omitted. For example, Ahmad et al. [21] performed a CFD simulation involving sodium chloride as a solute to examine CP and mass transfer coefficients in narrow channels. By assuming a constant permeate flux and constant mass fraction along the channel, they applied a laminar flow model to a two-dimensional domain. While they utilized User-Defined Functions (UDFs) in the ANSYS Fluent solver to improve the accuracy of the film theory description, their simulation was limited by the assumption of a constant permeate flux along the membrane length.

Pak et al. [22] addressed this by developing a two-dimensional numerical model that integrated continuity and momentum equations with Darcy's law, indicating that a variable permeation flux yields results that align more closely with experimental observations. Similarly, Lotfiyan et al. [23] conducted 2D CFD modeling using an Eulerian multiphase approach and Darcy's equation. Their findings highlighted a non-linear relationship between TMP and permeate flux for oil-in-water emulsions, noting that increased TMP led to higher concentrations at the membrane surface. Despite accounting for droplet interactions, a significant gap remained between their simulations and experimental flux data, which was attributed to the exclusion of pore-blocking effects [24].

Subsequent work by Behroozi et al. [25] demonstrated that incorporating macroscopic pore-blocking phenomena improved alignment with experimental values by approximately 15%.

Further studies using 3D CFD models have evaluated oil removal efficiency, achieving up to 88% efficiency with hydrophilic PTFE membranes [26]. These models confirmed that while increasing oil concentration elevates TMP due to fouling, aeration can mitigate these effects by generating high shear forces along the membrane surface. Research has also clarified that surface chemistry and wettability are often more critical than operating pressure [27]. Furthermore, the interaction between oil droplets and membrane pores is highly dependent on surface tension and contact angle, where droplet coalescence at pore openings can overcome capillary barriers and lead to decreased rejection [28,29].

This research develops a simulation framework within ANSYS Fluent based on the Eulerian–Eulerian multiphase model. This approach was specifically selected because it solves independent continuity and momentum equations for each phase, which is essential for capturing the complex interactions between oil droplets and water flow at the membrane surface. Rather than employing a conventional porous media zone with defined thickness, the study utilizes a zero-thickness wall boundary condition where the water permeation is governed by a velocity-based Darcy formulation. The framework incorporates custom User-Defined Functions (UDFs) to dynamically adjust the flow according to the local oil volume fraction at the wall. This effectively accounts for both oil accumulation and back-diffusion, providing a more efficient method for modeling membrane transport.

The primary objective of this study is to develop a 2D CFD model where the membrane is represented as a simplified wall interface, using the intrinsic experimental water resistance (Rm) as the constant input. By coupling the oil concentration at the wall with the permeation rate through specialized C-language code, the model mimics the behavior of a physical membrane. To ensure the reliability of the framework, the initial simulation was validated against experimental results from steady-state cases, confirming that the numerical model is accurate and capable of predicting real-world behavior. Furthermore, the research examines the formation of the initial fouling layer and the resulting flux decline under various hydrodynamic conditions, including different oil concentrations and droplet sizes. Ultimately, this validated framework serves as a predictive tool for analyzing operational parameters that would otherwise necessitate expensive and complex laboratory

experiments, thereby demonstrating its utility in optimizing membrane performance while reducing the reliance on physical trials.

2. Methods

In the research, an experimental and numerical setup was used to investigate and enhance the operational parameters that might affect the membrane treatment behavior. The main principle that governs the membrane behavior of the flux across the membrane is Darcy's Equation (1), where the flux across the membrane is directly proportional to the transmembrane pressure (*TMP*) across the membrane and inversely proportional to the resistance of the membrane (*R*) to the flux across it.

$$J = \frac{TMP}{R} \tag{1}$$

2.1. Experimental Setup

Significant experimental research has been conducted on membrane treatment, encompassing a broad range of pore sizes, solutes, and operational parameters to evaluate separation performance. In the field of oil–water treatment, several studies have adopted methodologies comparable to those utilized by Behroozi et al. [25], Lotfiyan et al. [23], and Pak et al. [22]. The present study adhered to a similar methodological framework when performing the experiments, even though some previous experimental configurations were more sophisticated.

The experimental setup was built with the aim of taking the resistance value of a certain membrane without going into detail about the suitable model to find the membrane resistance value. Membrane resistance can be divided into two main components: the water membrane resistance (R_m), which is the resistance of the membrane to only passing through without any contaminants, and the fouling resistance ($R_{fouling}$), which includes all the types of fouling that might occur due to the oil presence. The two terms of the membrane resistance can then be added to form the total membrane resistance (R_{total})

In the experiment, a 0.5 hp centrifugal pump (OKAYING-VX-60) was used to produce pressure head to create the flux across the membrane. The experimental schematic setup is shown in Figure 2, where a combination of manual valves, pressure gauges, and a flow meter to control the operational parameters.

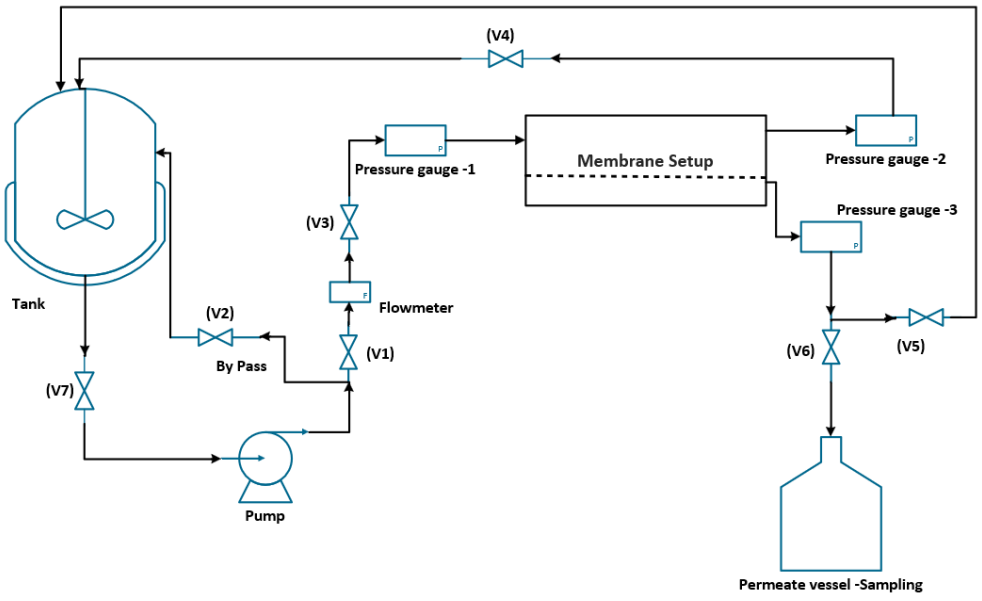

Figure 2. Schematic of the experimental setup used in the research.

When taking the values of flux at each TMP, the flow rate must be fixed at a certain value. A constant sample volume is taken while measuring the time needed to fill the sample. With those values and having a constant membrane area, the flux is determined at each operating point. Following the previously established methodology, oil volumes of 60 mL and 120 mL were incrementally added to approximately 12 L of water to achieve concentrations of 0.5% and 1.0% oil, respectively. To ensure the oil was fully emulsified into fine droplets, 10 g and 20 g of Sodium Dodecyl Sulfate (SDS) were incorporated into the mixture.

Flow rate and operating parameters are manually regulated using a series of valves, with system performance inherently constrained by the characteristic pressure–flow curve of the centrifugal pump. The primary flow path extends from the feed tank to the pump and through valve (V_1), which controls the flow entering the membrane module. A bypass line upstream of (V_1), equipped with valve (V_2), serves multiple functions, including flow stabilization during pump start-up and pressure regulation in the main line by adjusting the flow circuit.

Additional pressure control is achieved through valves located along the retentate line. A flow meter and pressure gauge (P_1) monitor the inlet flow conditions, while a pressure gauge (P_2) measures the pressure at the module outlet. The pressure gauge (P_3) is used to monitor the permeate-side pressure. Downstream of (P_3), the permeate stream is divided into two paths: one regulated by valve (V_5), which returns flow to the feed tank, and a second controlled by valve (V_6), which allows permeate collection for volume sampling and flux calculation using Equation (2) where (V), the permeate volume, (A) the membrane area, and (Δt) is the total time to fill the vessel volume.

$$J = \frac{V}{A \times \Delta t} \tag{2}$$

To determine the flux at each transmembrane pressure (TMP) level, the flow rate was maintained at a fixed value. A consistent sample volume was collected while the time required to fill the container was recorded. Using these two measurements and the known membrane surface area, the flux was calculated for every operating point. Following the previously established methodology, oil volumes of 60 mL and 120 mL were added incrementally to approximately 12 L of water to reach concentrations of 0.5% and 1.0%, respectively. To ensure the oil was fully emulsified into fine droplets, 10 g and 20 g of Sodium Dodecyl Sulfate (SDS) were incorporated into the mixture. Additionally, a 0.5 HP centrifugal pump operating at approximately 3000 rpm was utilized to assist with the mixing and emulsification process.

The experimental setup for the membrane was designed with the numerical setup in mind. The CFD model was chosen to be a two-dimensional model to reduce the computational cost. Therefore, the membrane mode was selected to be a flat sheet, where the inlet flow was designed to approximate an infinite-plate flow condition by introducing the feed through a slot-shaped inlet. The module consists of two main components: a top and a bottom shell. The membrane is positioned in a dedicated groove within the bottom shell, which also includes a 3 mm groove for an O-ring to prevent leakage. The top shell is designed without grooves and applies uniform compression to securely seal the module.

The internal flow channel (membrane length) has a length of 132 mm and a width of 65 mm, with both the top and bottom shells having a depth of 50 mm. Slot openings are located on both sides of the membrane to ensure crossflow operation and avoid dead-end filtration. To connect the module to the hydraulic system, a transition holder was designed to convert the circular hose flow into a slot-like flow profile. The entire assembly was fabricated using 3D-printed PETG filament and secured with threaded metal rods and

nuts to provide structural stability. To support the membrane under operating pressure and prevent deformation or damage, a perforated metal sheet was placed beneath it, and sealant was applied during assembly to ensure a leak-free system. Figure 3 shows how the membrane module was held together and assembled. The experiments were done in a steady-state manner where the flow rate was kept at a constant value of 10.4 L/min.



Figure 3. Assembly of the experimental membrane module setup.

2.2. Mathematical Modeling and Numerical Solution

Due to having multiple fluids in the system, the regular Navier–Stokes equations are not sufficient to represent the model. ANSYS Fluent 2019 R3 provides three multiphase models to choose from when dealing with multiple fluids: the Volume of Fluid (VOF), Mixture, and Eulerian models [30]. For the scope of this research, emulsified oil droplets in water treatment using membrane technology were investigated. The Eulerian-Eulerian multiphase model was selected.

Unlike the Mixture model, the Eulerian approach solves separate continuity and momentum equations for each phase while enforcing a shared pressure field, allowing for a more general and robust representation of phase interactions. Although more computationally demanding, the Eulerian model is better suited for cases where dispersed-phase behavior is uncertain, phase distributions may be nonuniform, and oil droplets may interact strongly with shear flow and membrane surfaces.

The main assumptions considered in the model are listed below:

(a) The model is two-dimensional,
(b) Steady-state behavior is assumed,
(c) Both oil and water are incompressible,
(d) The membrane does not allow any oil (full oil rejection).

The assumptions made in each model element are mentioned below with the model description.

A macroscale approach was adopted to model membrane behavior, treating the membrane as a porous medium and describing water permeation using Darcy's law. In the multiphase formulation, the permeate flux was scaled by the water volume fraction, and

membrane resistance was expressed as the product of water viscosity and resistance, yielding a velocity-based Darcy formulation as in Equation (3).

$$v_{Darcy} = \frac{TMP \cdot \alpha_w}{\mu_w \cdot R_m} \tag{3}$$

The effects of concentration polarization and backward diffusion were incorporated into the membrane model using a custom User-Defined Function (UDF) expressed in Equation (4). Concentration polarization was modeled through an effective increase in membrane resistance, while backward diffusion was represented by a velocity term proportional to the wall-normal gradient of the local oil volume fraction and the effective molecular diffusivity of oil (D_{eff}) in water (m^2/s). The negative sign indicates that diffusion occurs in the direction opposing the concentration gradient.

$$v_{backward} = -D_{eff}\frac{dC}{dy} \tag{4}$$

Although backward diffusion physically represents solute (oil) transport, it is incorporated here as a macroscopic correction to the pressure-driven permeation velocity. This approach reduces the effective solvent permeation rate in regions of elevated oil concentration, thereby accounting for concentration polarization without explicitly solving a separate solute transport equation, and the local membrane mass flux is expressed accordingly in Equation (5).

$$J = \left(v_{Darcy} + v_{backward}\right) \cdot \rho_w \tag{5}$$

The permeate flux is implemented as a mass source term in the continuity equations, combining the pressure-induced flow and the resistance due to concentration at the surface. The membrane was set as a wall-type boundary where a sink term on the feed side of the membrane and as a source on the permeate side, using User-Defined Functions (UDFs) written in C language and compiled into ANSYS Fluent. This implementation allows the source term to be applied locally to each membrane adjacent cell and updated during each solver iteration based on local flow variables, enabling spatially and temporally resolved modeling of membrane transport behavior.

Since the multiphase model was chosen to be the Eulerian model, two continuity equations and two momentum equations were solved in addition to the total volume fraction equation. The source term (S_w) is usually zero, but in our case, this will be the source term used to mimic the membrane behavior.

$$Continuity = \begin{cases} \left(\frac{\partial}{\partial t}(\alpha_w \rho_w) + \nabla \cdot \left(\alpha_w \rho_w \vec{\boldsymbol{u}}_{\boldsymbol{w}}\right) = S_w\right) \cdot \frac{1}{\rho_{rw}} \\ \left(\frac{\partial}{\partial t}(\alpha_o \rho_o) + \nabla \cdot \left(\alpha_o \rho_o \vec{\boldsymbol{u}}_{\boldsymbol{o}}\right) = S_o\right) \cdot \frac{1}{\rho_{ro}} \end{cases} \tag{6}$$

$$Momentum = \begin{cases} \frac{\partial}{\partial t}\left(\alpha_w \rho_w \vec{\boldsymbol{u}}_w\right) + \nabla \cdot \left(\alpha_w \rho_w \vec{\boldsymbol{u}}_{\boldsymbol{w}} \vec{\boldsymbol{u}}_{\boldsymbol{w}}\right) = -\alpha_w \nabla p + \nabla \cdot [\alpha_w \boldsymbol{\tau}_w] + \alpha_w \rho_w \vec{\boldsymbol{g}} + \sum \vec{\boldsymbol{F}}_{\boldsymbol{w}} \\ \frac{\partial}{\partial t}\left(\alpha_o \rho_o \vec{\boldsymbol{u}}_o\right) + \nabla \cdot \left(\alpha_o \rho_o \vec{\boldsymbol{u}}_{\boldsymbol{o}} \vec{\boldsymbol{u}}_{\boldsymbol{o}}\right) = -\alpha_o \nabla p + \nabla \cdot [\alpha_o \boldsymbol{\tau}_o] + \alpha_o \rho_o \vec{\boldsymbol{g}} + \sum \vec{\boldsymbol{F}}_{\boldsymbol{o}} \end{cases} \tag{7}$$

$$\sum_{i=1}^{n} \alpha_i = 1 \tag{8}$$

$$\alpha_w + \alpha_o = 1 \tag{9}$$

The term ($\sum \vec{\boldsymbol{F}}$) is the sum of various interfacial forces like (drag force, lift force, wall lubrication, virtual mass force, etc.). Equation (10) shows the detailed terms of the interfacial forces, where the term ($K_{ow}\left(\vec{\boldsymbol{u}}_{\boldsymbol{o}} - \vec{\boldsymbol{u}}_{\boldsymbol{w}}\right)$ represents the interphase forces between the phases,

like pressure, cohesion, and other effects, (K_{ow}) is the interphase momentum coefficient between primary phase (w) and secondary phases (o).

$$\sum \vec{F_w} = \sum_{i=1}^{n} \left(K_{ow} \left(\vec{u}_o - \vec{u}_w \right) + \dot{m}_{ow} \vec{u}_{ow} - \dot{m}_{wo} \vec{u}_{wo} \right) + \left(\vec{F}_{ext} + \vec{F}_{lift,w} + \vec{F}_{vm,w} \right) \quad (10)$$

Due to the multiphase nature of the case, parameters that govern and describe the phase interaction need to be defined. One of these parameters is the virtual mass term, which represents the mass the particle sees when it accelerates, pushing the surrounding fluid, making the particle behave as if it has extra mass [30]. This matters most when the fluid is as dense or denser than the particle. The force equation for virtual mass is shown in Equation (11)

$$\vec{F}_{vm,w} = C_{vm} \cdot \rho_w \cdot \boldsymbol{V_w} \cdot \boldsymbol{a_r} \quad (11)$$

where ($\boldsymbol{a_r}$) is the relative acceleration of the particle (oil phase) relative to the primary phase (water), and (C_{vm}) is called the virtual mass coefficient. This coefficient represents the particle volume of displaced fluid that contributes to the effective virtual mass of the particle, in terms of a fraction of the particle volume. In very dilute bubbly flows (volume fraction < 0.3), using the constant value 0.5 is a typical and reasonable baseline [30]. Therefore, it is reasonable to choose a constant value of 0.5 for a virtual mass coefficient. Especially when the model we are dealing with has small volume fractions, and there are no big pressure gradients in the flow, in addition to having to deal with more stable and less computational costs.

The drag force is considered to be an interfacial/interphase exchange force where the exchange coefficient (K_{ow}) for flow types of bubbly, liquid–liquid, or gas–liquid mixtures as described in Equation (12). Where (f) represents the drag function, (τ_o) is the nondimensional droplet relaxation time represented in Equation (13), and (A_o) as the interfacial area, which is defined as the interfacial area between two phases per unit mixture volume, and (d_o) is the droplet diameter. For the interfacial area, the model to describe it was chosen to be the particle model represented in Equation (14).

$$K_o = \frac{\rho_o \cdot f}{6\tau_o} d_o A_o \quad (12)$$

$$\tau_o = \frac{\rho_o \cdot {d_o}^2}{18\mu_o} \quad (13)$$

$$A_o = \frac{6\alpha_o}{d_o} \quad (14)$$

The Schiller–Naumann model is a good approximation for spherical particles and bubbles. This model depends on the values of the Reynolds number for the droplets of the secondary phase. The maximum droplet diameter will be (100 μm), and the relative velocity ($\left| \vec{u}_o - \vec{u}_w \right|$) between the phases in the Eulerian model is a very small order of (10^{-3}–10^{-6}), which will lead to the maximum ($Re_{droplet}$) to be approximately 44. This means that the Reynolds number does not pass the threshold of 1000.

$$f = 1 + 0.15 \cdot {Re_{droplet}}^{0.687} \quad (15)$$

$$Re_{droplet} = \frac{\rho_w \cdot d_o \cdot \left| \vec{u}_o - \vec{u}_w \right|}{\mu_w} \quad (16)$$

The lift force on the particle is an important aspect in the model. Since the case is a liquid–liquid case, the two recommended models to choose from are the Saffman and the

Legendre–Magnaudet lift model [31,32]. No difference was noticed when comparing the two, so the Saffman model (Equation (17)) was chosen to reduce the computational cost and time [33].

$$\vec{F}_{lift,o} = -C_{lift} \cdot \rho_o \alpha_o \left(\vec{u}_o - \vec{u}_w \right) \times \left(\nabla \times \vec{u}_o \right) \quad (17)$$

The lift forces and virtual mass force for each phase are the same value but opposite direction, ($\vec{F}_{lift,o} = -\vec{F}_{lift,w}$) and ($\vec{F}_{vm,w} = -\vec{F}_{vm,o}$).

Since the scope of the paper did not consider the change in temperature inside the fluid, the surface tension was kept constant at a value of 0.035 (N/m), and the Continuum Surface Force option was chosen since there are no temperature gradients.

Second-order upwind schemes for momentum and scalars, Modified HRIC for interface tracking, and second-order pressure discretization combined provided a numerically stable and high-accuracy solution for Eulerian oil–water flow simulations.

To approximate these membrane-scale mechanisms on a macroscopic CFD grid, a custom UDF was written to impose the appropriate transport equations and flux relations at the membrane boundary and feed-side boundary layer.

The UDF system in Fluent is organized around a set of macro functions, each designed to execute at a specific point during a solver iteration. Two macro types are central to the membrane model: DEFINE_ADJUST and DEFINE_SOURCE. Figure 4 shows the UDF code execution.

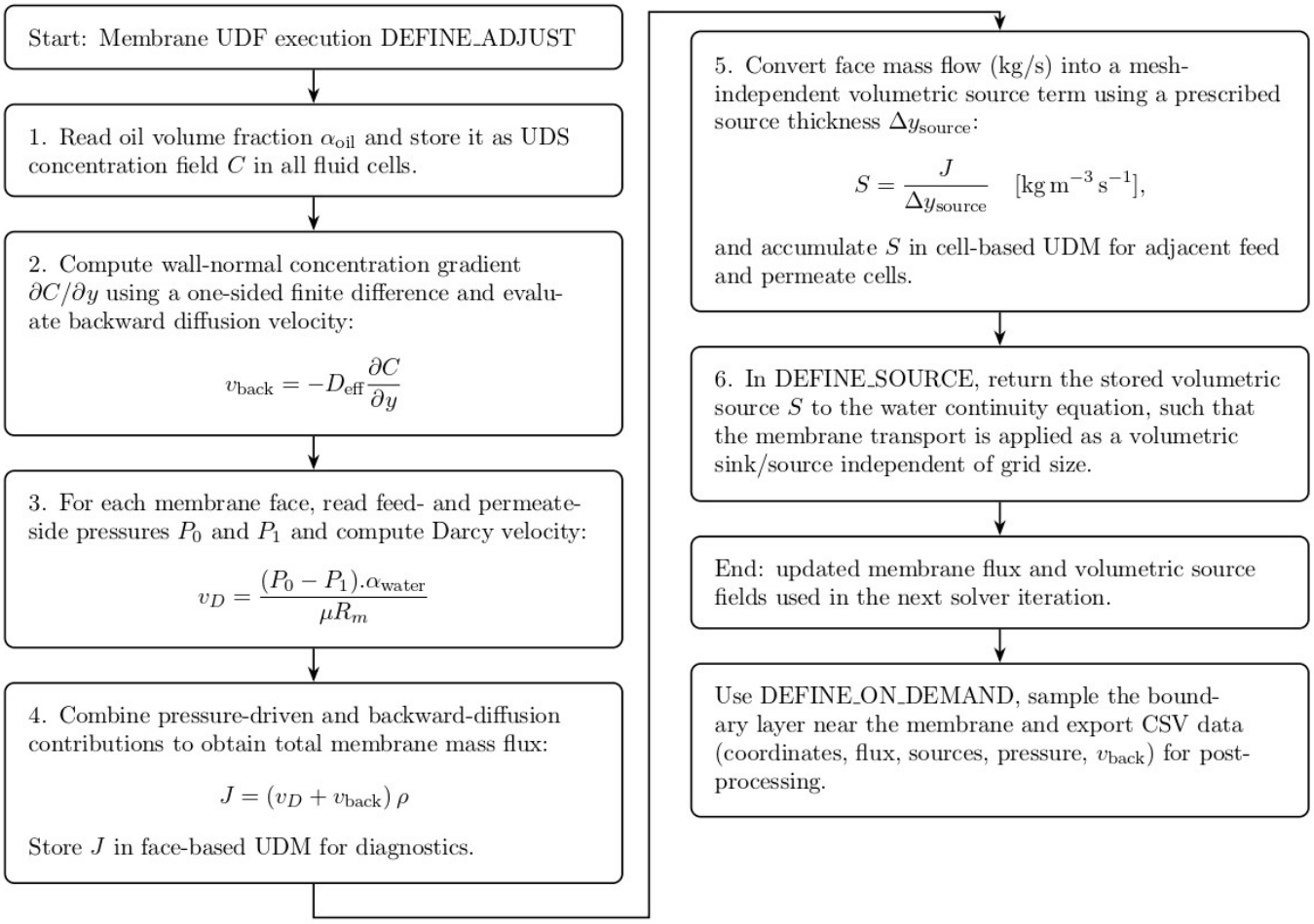

Figure 4. Flowchart of the (UDF) used to model the multiphase model.

3. Results and Discussion

In the experiment part, two main cases were investigated: pure water flow, 0.5%, and 1.0% oil to water v/v ratio. The pure water was used to extract the membrane water resistance, while the other was used to investigate the fouling and compare it with the numerical simulation.

3.1. Case for Pure Water Experiment and Numerical Model Validation

Each experiment was carried out at a constant TMP case while keeping the flow rate of the water at 10.5 L/min. The value for each case is shown in Table 1. Several trials were conducted in order to make sure the values are accurate, and the maximum standard deviation was 0.0192. The results were then plotted in order to determine the value of the membrane water resistance using Equation (18). Membrane water resistance was determined to be 6.46×10^{10} (1/m).

$$R\left[\frac{1}{\mathrm{m}}\right] = \frac{\rho_{water}}{\mu_{water}[\mathrm{Pa{\cdot}s}] \times Slope\left[\frac{\mathrm{kg}}{\mathrm{Pa{\cdot}m^2{\cdot}s}}\right]} \tag{18}$$

Table 1. Experimental readings for pure water flux at different TMP.

TMP (Bar)	Time (s)	Permeate Flux (kg/m^2·s)	Average Flux (kg/m^2·s)	Standard Deviation
0.15	52	0.343	0.342	0.0023
	51.8	0.344		
	52.5	0.340		
0.35	26	0.686	0.687	0.0067
	26.2	0.681		
	25.7	0.694		
0.45	20.8	0.857	0.853	0.0075
	20.7	0.861		
	21.1	0.845		
	21	0.849		
0.6	17.5	1.019	1.095	0.0058
	17.6	1.013		
	17.4	1.025		
0.85	14.3	1.247	1.241	0.0192
	14.1	1.265		
	14.6	1.221		
	14.5	1.230		

The experiment was validated by extracting the membrane water resistance and adding the value to the numerical setup. The results were in alignment with the trendline of the experimental data, as shown in Figure 5.

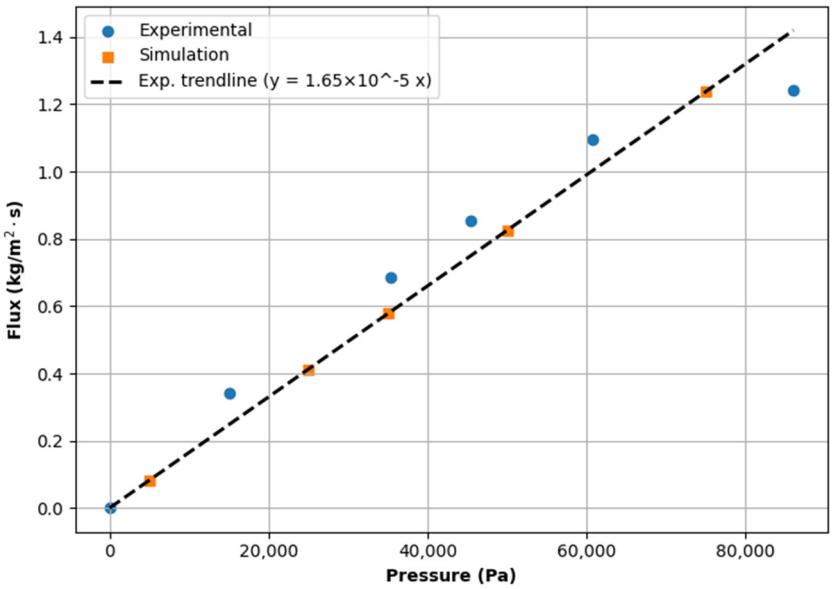

Figure 5. Experimental and numerical results for pure water flux.

3.2. Case for 0.5%and 1.0% Oil-in-Water Experiment and Numerical Validation

Following the previously established methodology, oil volumes of 60 mL and 120 mL were incrementally added to approximately 12 L of water to achieve concentrations of 0.5% and 1.0% oil, respectively. To ensure the oil was fully emulsified into fine droplets, 10 g and 20 g of Sodium Dodecyl Sulfate (SDS) were incorporated into the mixture. The experimental findings across three distinct transmembrane pressure (TMP) points are summarized in Table 2, where each collected sample maintained a consistent volume of 1.5 L. Additionally, the mixing process was facilitated by a 0.5 HP centrifugal pump operating at a speed of roughly 3000 rpm, which ensured the uniform distribution and emulsification of the oil phase within the solution.

The validation of the data was done by keeping the membrane water resistance in the numerical setup and seeing what happens when the oil is introduced into the flow. The results are plotted in Figure 6, where the data had good alignment with the experimental results.

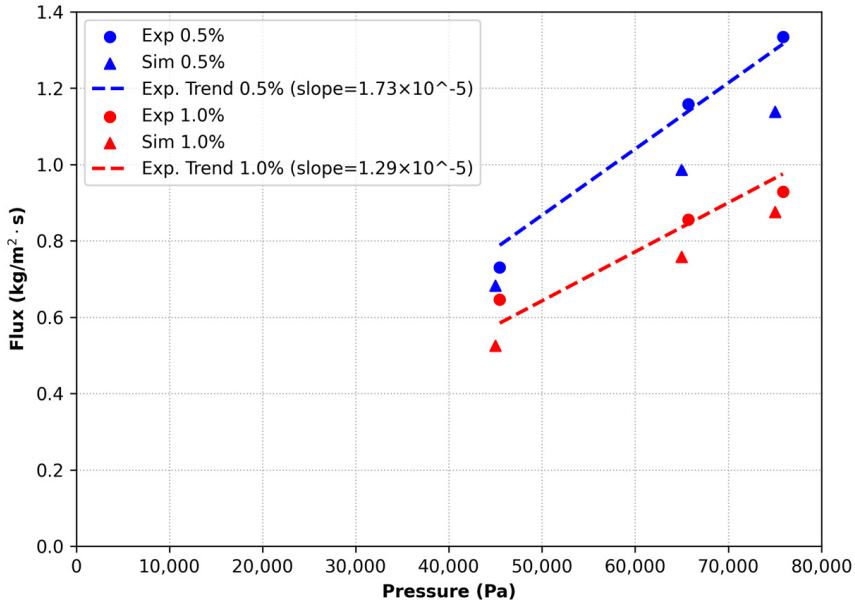

Figure 6. Experimental and numerical results for 0.5% and 1.0% oil to water v/v.

Table 2. Experimental results for 0.5% and 1.0% oil to water v/v.

	TMP (Bar)	Time (s)	Flux (kg/m^2·s)	Average Flux	Standard Deviation
0.5% oil	0.45	24.4	0.731	0.7301	0.0056
		24.3	0.734		
		24.7	0.722		
		24.3	0.734		
	0.75	13.4	1.331	1.334	0.0153
		13.5	1.321		
		13.2	1.351		
	0.65	15.6	1.143	1.158	0.0150
		15.2	1.173		
		15.4	1.158		
1.0% oil	0.45	27.3	0.653	0.6455	0.00565
		27.6	0.646		
		27.8	0.641		
	0.75	18.9	0.943	0.929	0.0145
		19.5	0.914		
		19.2	0.929		
	0.65	20.5	0.870	0.855	0.00144
		21.2	0.841		
		20.9	0.853		

3.3. Mesh Independence Study for Numerical Model

In order to make sure that the values and results that were taken from the simulation have very small truncation error and the mesh size does not play a role in the simulation results different number of mesh were simulated and found that there are no big difference in the result of 13,200 mesh are similar to 26,400 mesh, so the mesh number was taken 13,200 to reduce the computational cost. This can be shown in the fluxes at different TMP Figure 7a and the oil boundary layer along the membrane Figure 7b that plays a big role in the simulation results.

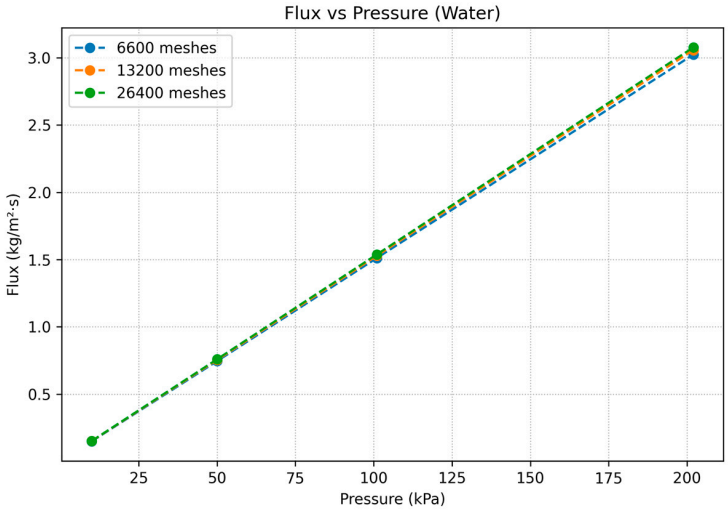

(**a**)

Figure 7. *Cont.*

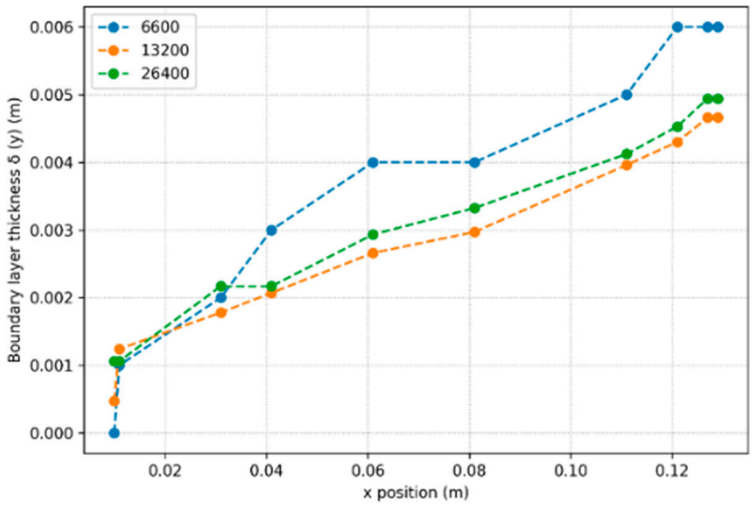

(**b**)

Figure 7. Mesh independence study for different numbers of meshes (**a**) flux comparison and (**b**) oil boundary layer comparison.

3.4. Effect of Transmembrane Pressure

The numerical parameters were set to an inlet velocity of 0.116 m/s, an inlet oil volume fraction of 0.023, and a constant oil droplet diameter of 100 µm. It is noticed from Figure 8 that the oil boundary layer or the oil distribution above the membrane is not affected by the TMP applied to it.

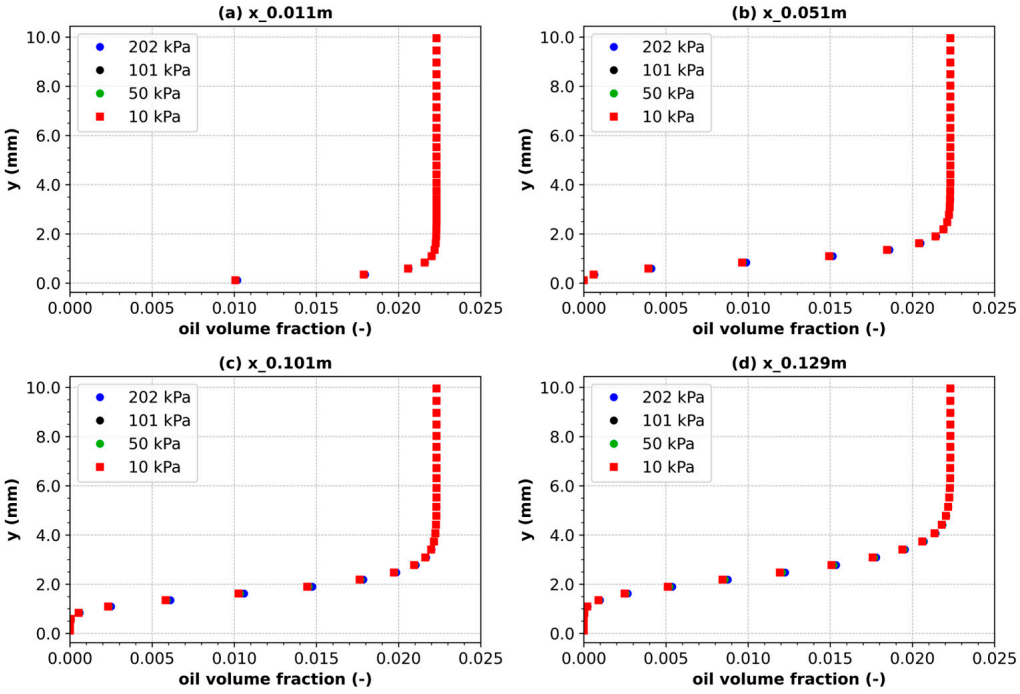

Figure 8. Effect of different TMP on the oil boundary layer distribution along the membrane.

3.5. Effect of Inlet Velocities

In order to determine the effect of changing the inlet velocity was fixing other operational parameters being, TMP of 202 kPa, inlet oil volume fraction 0.0223, oil droplet diameter 100 µm while the velocity values were the flux along the membrane for different velocities is shown in Figure 9. The results show that increasing the velocity had a negative effect on the flux along the membrane. Initially thought that having more velocity would

increase the flux because it would reduce the boundary layer thickness. Further investigation showed that the oil distribution along the membrane was the reason that the flux was reduced, because the flux in the UDF code was a function of the volume fraction of the water in the cells near the membrane wall.

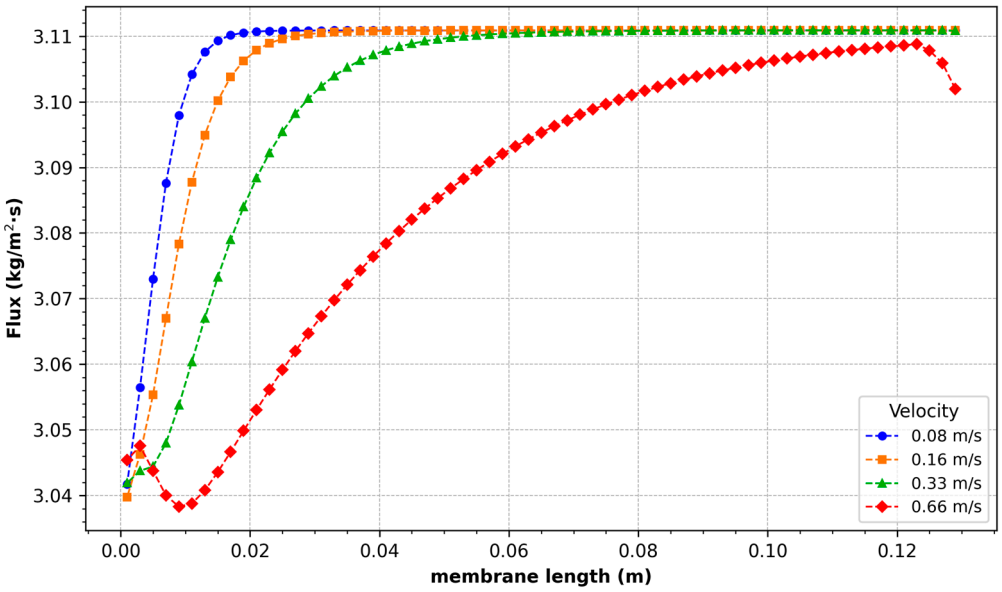

Figure 9. The effect of different velocities on the flux along the membrane.

In addition to the presence of the oil along the membrane, the backward diffusion also played a small role in the effect of the water flux through the membrane. This is shown in Figure 10, where the backward diffusion flux effects increased for higher velocities along the membrane.

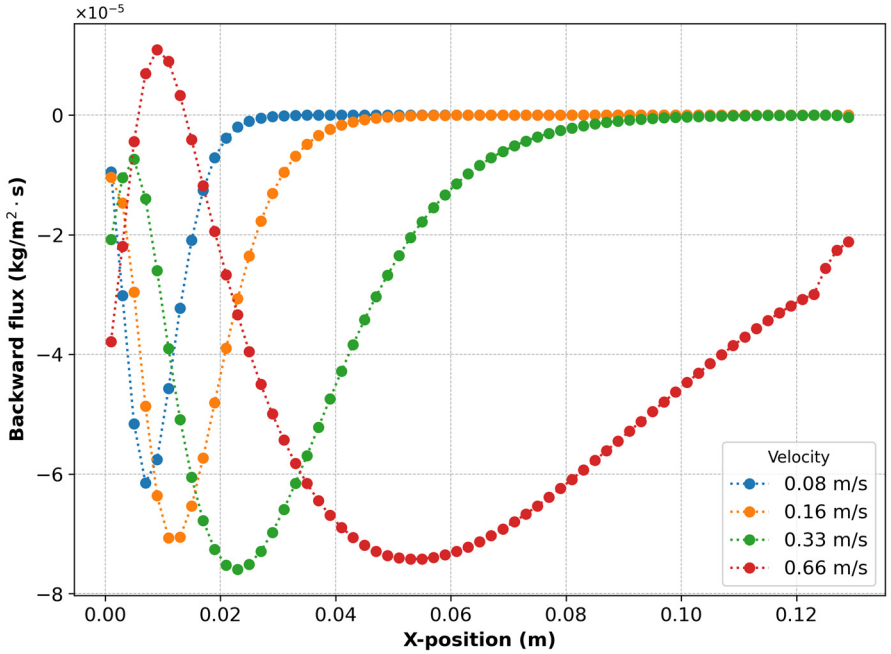

Figure 10. The effect of backward diffusion along the membrane for different velocities.

Having lower velocities resulted in the rise of oil droplets above the membrane and moving away. This is due to the buoyancy force being greater at lower velocities than the convectional force, which leads to oil moving away from the membrane.

3.6. Effect of Droplet Diameters

In the oil-treatment industry, the oil in the tertiary treatment is usually present in droplets of several diameters. These diameters have different effects on the operation of the membrane, where the large diameters might settle on the membrane and either block the pores completely or partially, while droplets smaller than the pores might pass or enter the pores and settle inside. Therefore, the behavior of the droplets from a macro point of view is important. The parameters are fixed at TMP 202 kPa, velocity 0.116 m/s, and oil concentration of 0.0223.

Results show that for the flux along the membrane for oil diameters 100 and 50 µm, the flux rises in a fast manner until it reaches the maximum level, while diameters 10, 5, 1 µm remain at a value of 3.03 (kg/m^2·s) where the oil volume fraction is around 2% and drops for some length of the membrane and then rises gradually till it reaches the maximum flux where there is no oil present on the membrane.

In Figure 11, it is noticeable that when decreasing the droplet size from 100 µm to 10 µm, the flux takes a longer part of the membrane length until it rises to the peak. However, when decreasing the oil droplet further from 10 µm to 5 µm, the flux does not decrease in the same manner. This might be due to the buoyancy forces on the larger droplets being greater, so the oil rises away from the membrane, which leads to higher water flux across it.

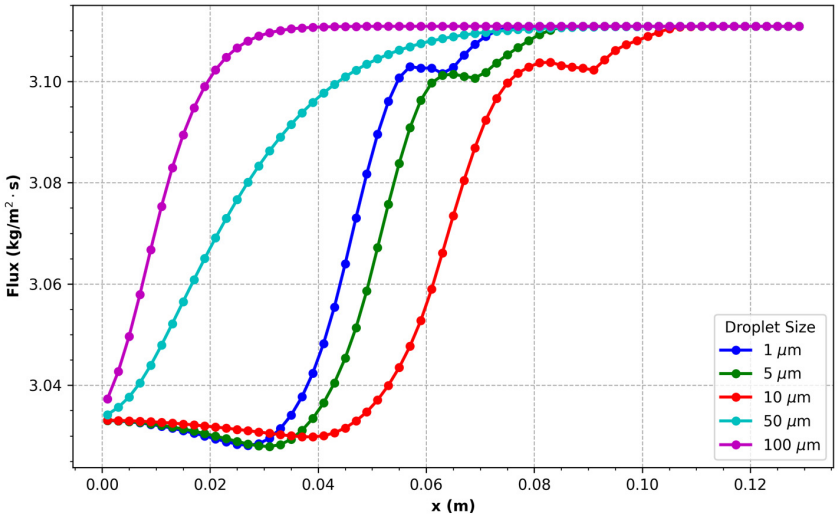

Figure 11. The effect of different oil droplet diameters on the flux along the membrane.

Due to the previous observation that the oil droplet behavior along the membrane is not affected by the pressure, and the oil concentration has a very small effect, further investigations are done on the droplet's diameter behavior with respect to the velocity. For each droplet diameter, different velocities (0.08, 0.16, 0.33, 0.66) m/s were simulated while fixing other parameters to be 202 kPa and 0.0223 oil volume fraction.

From Figure 12, it was noticed that the reason the previous droplets (1 µm, 5 µm, 10 µm) behaved differently from (50 µm, 100 µm) at 0.116 m/s was that the convectional force from the feed velocity was strong when dealing with small droplets, which did not allow the droplets to move away from the membrane through the buoyancy force. However, it is noticed that by increasing the velocities, the larger droplet sizes (50 µm, 100 µm) started to settle more on the membrane feed side. The reason behind it is that larger droplets are more susceptible to internal lift forces, while smaller droplets at high velocities are being driven towards the membrane surface, leading to higher concentration and lower flux. This is also supported by the fact that at low velocity (0.08 m/s), the flux reaches a steady value fast, which implies that the crossflow is not large enough.

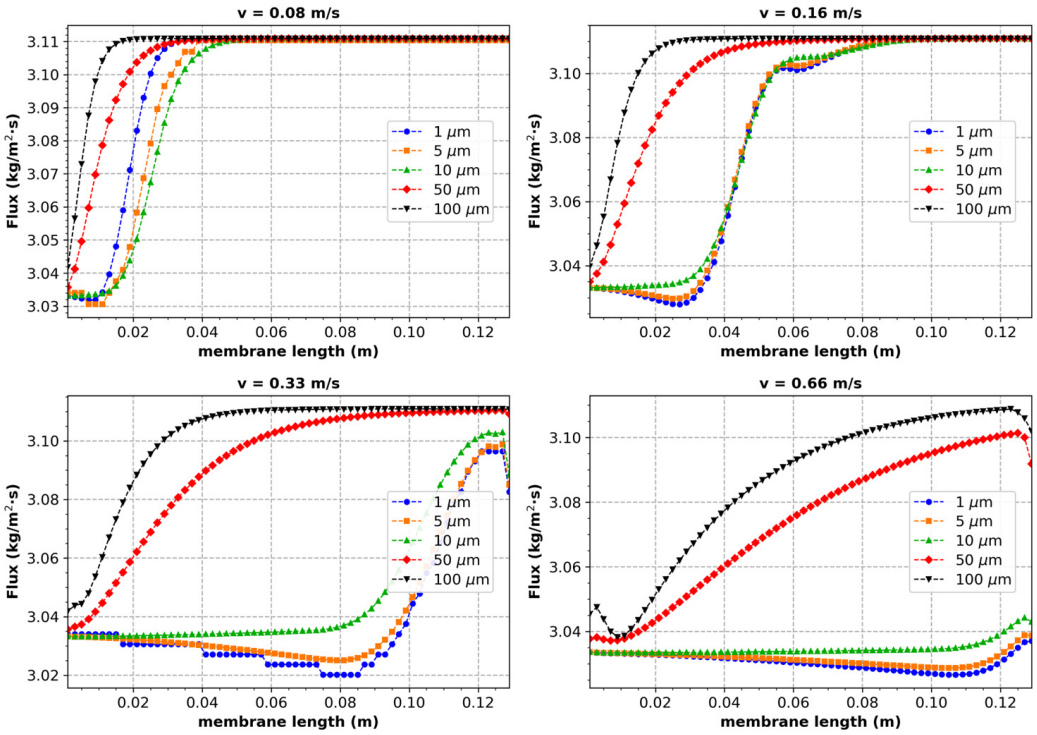

Figure 12. The flux distribution along the membrane for different oil droplet sizes at different velocities.

Previously, from the literature, the effects of velocity were mainly mentioned in the backward diffusion effect of the boundary layer on how the oil droplets might behave, but further investigation showed that the convection forces might play a larger role than the backward diffusion effect (concentration polarization). This is clearly shown in how the changing velocity governed how the oil droplets either settled along the membrane or were lifted away due to buoyancy forces. Figure 13 shows the total flux across the membrane at each velocity and each droplet size mentioned.

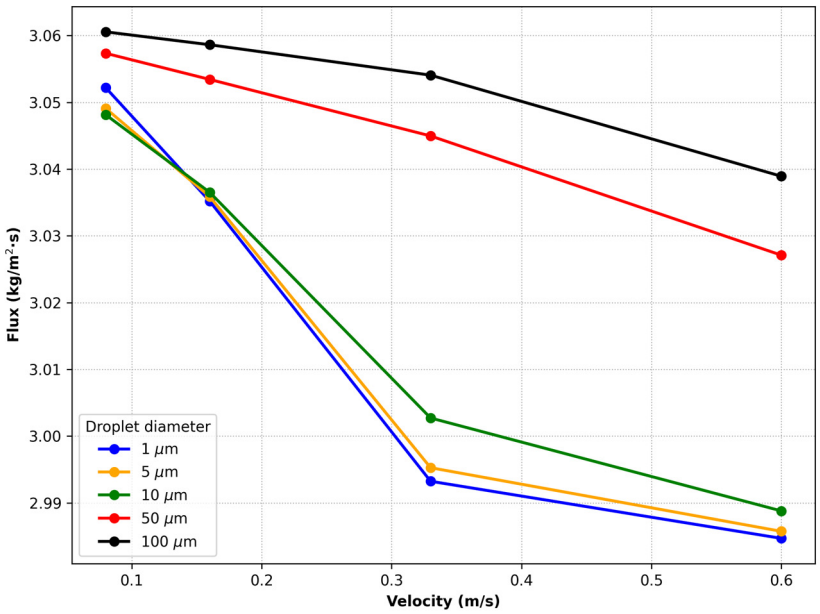

Figure 13. Total flux across the membrane for different oil droplets and different velocities.

3.7. Effect of Oil Concentrations

Another parameter that was aimed to be studied was the oil concentration that enters the membrane model, and see how the concentration affects the distribution along the membrane. The parameters were fixed to a TMP of 202 kPa, 0.116 m/s velocity, and 100 µm diameter. Figure 14 shows that the general behavior of the different oil concentrations was the same. The difference was that the flux rose from a low value to the maximum value for each case at a different rate. Where multiplying the v/v concentration of the multiplying was from 1% to 8% showed that the flux settled to the maximum value from 20 mm to 40 mm.

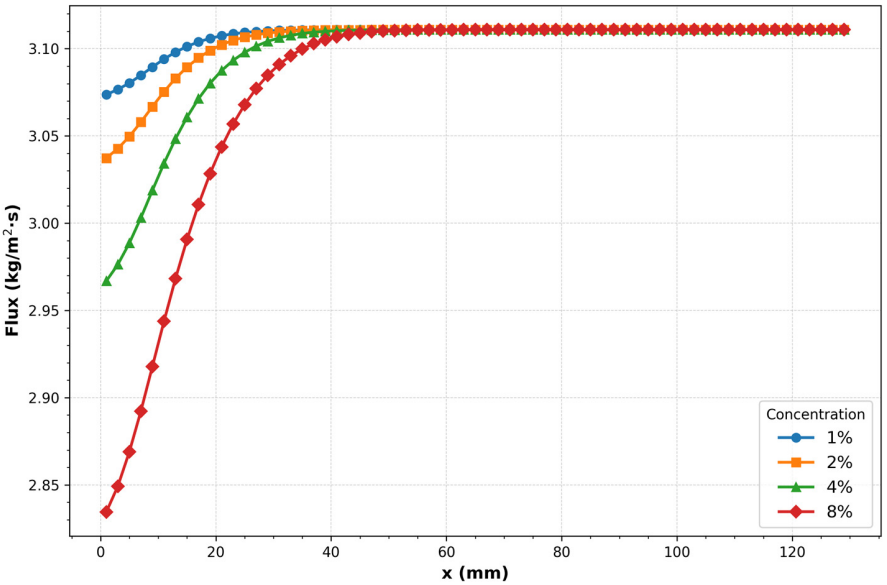

Figure 14. Flux distribution along the membrane for different oil concentrations.

To compare how the boundary layer is influenced by various concentrations, the oil volume fraction along and above the membrane was normalized relative to either the inlet or bulk oil volume fraction. Figure 15 illustrates that the oil boundary layers for different concentrations remain consistent along the membrane until reaching the midpoint. Beyond this point, oil droplets at higher concentrations migrate away from the membrane surface more rapidly.

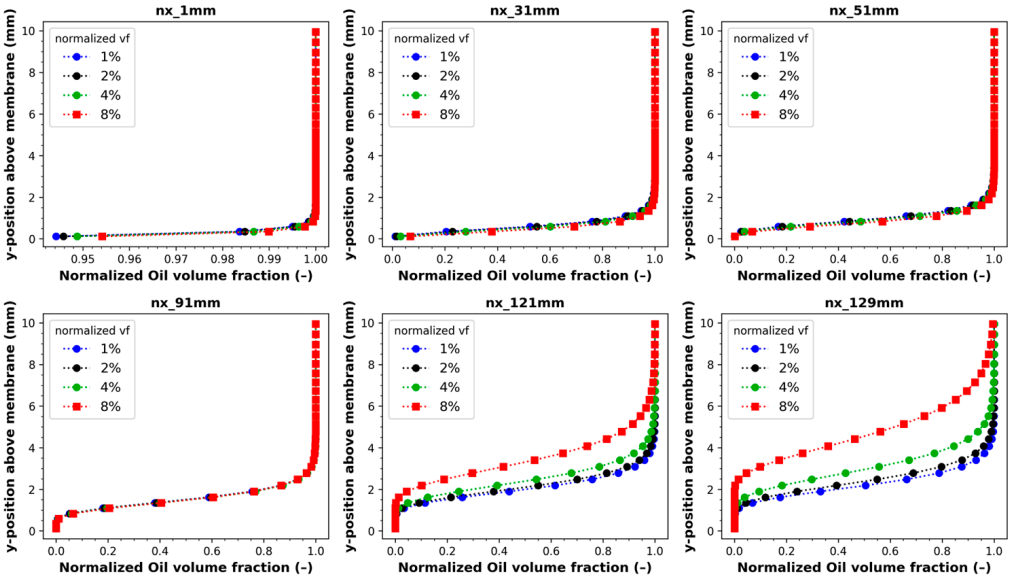

Figure 15. Normalized oil boundary layer at different x positions along the membrane for different inlet oil concentrations.

This phenomenon may be attributed to increased droplet interaction at higher concentrations, where droplets coalesce to form larger units. These larger droplets likely experience greater buoyancy forces due to their increased volume. However, this hypothesis could not be verified because a limitation of the Eulerian model is that individual droplets cannot be tracked. This is because the model treats all phases as an averaged continuum on a macroscopic level rather than on a discrete particle-particle basis.

4. Conclusions

We examined the effects of key operational parameters on membrane performance in oil–water separation systems through a combination of CFD simulations and experimental validation. The influence of transmembrane pressure, inlet velocity, oil droplet diameter, and oil concentration on water flux along the membrane was systematically evaluated. Among these parameters, pressure was identified as the primary factor controlling flux, consistent with Darcy's law and established membrane transport theory. While existing literature often emphasizes the role of velocity in enhancing backward diffusion and reducing concentration polarization, the findings of this study suggest that convective forces can have a more pronounced impact on oil droplet behavior near the membrane surface. Changes in inlet velocity were shown to govern whether oil droplets accumulated along the membrane or were displaced away from it due to buoyancy and flow-induced forces. This indicates that backward diffusion alone does not fully explain flux behavior under the investigated operating conditions.

Higher inlet oil concentrations were found to promote droplet accumulation near the membrane inlet, while reduced deposition was observed toward the membrane outlet. This behavior was attributed to droplet clustering and coalescence, which resulted in larger droplets that were more readily transported away from the membrane surface. The combined effects of pressure, membrane length, and inlet oil volume fraction on flux distribution were summarized graphically, while the intertwined relationship between velocity and oil droplet diameter required joint analysis to clearly visualize their influence.

Although some discrepancies were observed between experimental and simulated results for pure water, 0.5% and 1.0% oil–water mixture, the numerical model showed good agreement with experimentally derived inputs, particularly the membrane water resistance incorporated into the simulations. These results support the applicability of the modeling approach within its defined assumptions.

Further studies could combine other multiphase modes to both simulate the hydrodynamic parameters and track the droplets. Another limitation of this study was that the wettability of the membrane could not be determined because of the limitations of the Eulerian-Eulerian model, where the surface interaction between the oil droplet and the water and membrane surface can be characterized. This might need another model to simulate the interaction between the oil droplet and the membrane surface, either by UDF code or another method of interaction.

Author Contributions: Conceptualization, A.S. and R.B.-M.; methodology, A.S. and R.B.-M.; software, A.S. and R.B.-M.; validation, A.S.; formal analysis, A.S. and R.B.-M.; investigation, A.S. and R.B.-M.; resources, R.B.-M.; data curation, A.S. and R.B.-M.; writing—original draft preparation, A.S. and R.B.-M.; writing—review and editing, A.S. and R.B.-M.; visualization, A.S.; supervision, R.B.-M.; project administration, R.BM.; funding acquisition, R.B.-M. All authors have read and agreed to the published version of the manuscript.

Funding: The authors would like to acknowledge the support provided by The KFUPM Consortium for a Sustainable Future under Project # SUFC 2301 to carry out this work. The support provided by the IRC for Sustainable Energy Systems, the Mechanical Engineering Department, and the Deanship of Research at KFUPM is equally acknowledged.

Institutional Review Board Statement: Not applicable.

Informed Consent Statement: Not applicable.

Data Availability Statement: The original contributions presented in the study are included in the article, further inquiries can be directed to the corresponding author.

Conflicts of Interest: The authors declare no conflict of interest.

Nomenclature

Symbol	Name	Unit
TMP	Transmembrane Pressure	Pa
R	Resistance of the membrane	1/m
J	Water flux across the membrane	$kg/(m^2 \cdot s)$
V	Sample volume	m^3
A	Membrane area	m^2
Δt	Sample time of filling the sample volume	s
v_{Darcy}	Darcy's velocity across the membrane	m/s
α_w	Water volume fraction	-
α_o	Oil volume fraction	-
μ_w	Water dynamic viscosity	Pa·s
R_m	Membrane water resistance	1/m
$R_{fouling}$	Membrane resistance due to fouling	1/m
R_{total}	The combination of the membrane water and fouling resistance	1/m
$v_{backward}$	Backward diffusion velocity	m/s
D_{eff}	Effective molecular diffusivity of oil in water	m^2/s
ρ_w	Water density	kg/m^3
ρ_o	Oil density	kg/m^3
$\vec{F}_{vm,w}$	Virtual mass force on water	N
$\vec{F}_{vm,o}$	Virtual mass force on oil	N
K_{ow}	Drag exchange coefficient between oil and water	-
f	Drag function	-
τ_i	Nondimensional droplet relaxation time	-
A_i	interfacial area	1/m
d_o	Oil droplet diameter	m
$Re_{droplet}$	Reynolds number for oil droplet	-
$\vec{F}_{lift,o}$	Lift force on oil phase	N
$\vec{F}_{lift,o}$	Lift force on oil phase	N
C_{lift}	Lift coefficient	-

References

1. Alagoz, E.; Alghawi, Y. The Energy Transition: Navigating the Shift Towards Renewables in the Oil and Gas Industry. *J. Energy Nat. Resour.* **2023**, *12*, 21–24. [CrossRef]
2. Calel, R.; Dechezleprêtre, A. Environmental Policy and Directed Technological Change: Evidence from the European Carbon Market. *Rev. Econ. Stat.* **2016**, *98*, 173–191. [CrossRef]
3. Jacobson, M.Z.; Delucchi, M.A.; Cameron, M.A.; Frew, B.A. Low-cost solution to the grid reliability problem with 100% penetration of intermittent wind, water, and solar for all purposes. *Proc. Natl. Acad. Sci. USA* **2015**, *112*, 15060–15065. [CrossRef]
4. McGlade, C.; Ekins, P. The geographical distribution of fossil fuels unused when limiting global warming to 2 °C. *Nature* **2015**, *517*, 187–190. [CrossRef]
5. Fakhru'l-Razi, A.; Pendashteh, A.; Abdullah, L.C.; Biak, D.R.A.; Madaeni, S.S.; Abidin, Z.Z. Review of technologies for oil and gas produced water treatment. *J. Hazard. Mater.* **2009**, *170*, 530–551. [CrossRef]
6. Ghafoori, S.; Omar, M.; Koutahzadeh, N.; Zendehboudi, S.; Malhas, R.N.; Mohamed, M.; Al-Zubaidi, S.; Redha, K.; Baraki, F.; Mehrvar, M. New advancements, challenges, and future needs on treatment of oilfield produced water: A state-of-the-art review. *Sep. Purif. Technol.* **2022**, *289*, 120652. [CrossRef]

7. Costa, T.C.; Hendges, L.T.; Temochko, B.; Mazur, L.P.; Marinho, B.A.; Weschenfelder, S.E.; Florido, P.L.; da Silva, A.; de Souza, A.A.U.; de Souza, S.M.A.G.U. Evaluation of the technical and environmental feasibility of adsorption process to remove water soluble organics from produced water: A review. *J. Pet. Sci. Eng.* **2022**, *208*, 109360. [CrossRef]
8. Saudi Arabian Oil Company (Aramco). *Saudi ARAMCO Annual Reports 2019–2024*; Saudi Arabian Oil Company (Aramco): Dhahran, Saudi Arabia, 2024.
9. Nasiri, M.; Jafari, I.; Parniankhoy, B. Oil and Gas Produced Water Management: A Review of Treatment Technologies, Challenges, and Opportunities. *Chem. Eng. Commun.* **2017**, *204*, 990–1005. [CrossRef]
10. Sonune, A.; Ghate, R. Developments in wastewater treatment methods. *Desalination* **2004**, *167*, 55–63. [CrossRef]
11. Madaeni, S.S. The application of membrane technology for water disinfection. *Water Res.* **1999**, *33*, 301–308. [CrossRef]
12. Ahmed, F.E.; Lalia, B.S.; Hashaikeh, R.; Hilal, N. Alternative heating techniques in membrane distillation: A review. *Desalination* **2020**, *496*, 114713. [CrossRef]
13. Liu, Y.; Lu, H.; Li, Y.; Xu, H.; Pan, Z.; Dai, P.; Wang, H.; Yang, Q. A review of treatment technologies for produced water in offshore oil and gas fields. *Sci. Total Environ.* **2021**, *775*, 145485. [CrossRef]
14. Cui, Z.F.; Jiang, Y.; Field, R.W. Fundamentals of Pressure-Driven Membrane Separation Processes. In *Membrane Technology: A Practical Guide to Membrane Technology and Applications in Food and Bioprocessing*; Elsevier: Amsterdam, The Netherlands, 2010; pp. 1–18. [CrossRef]
15. Keir, G.; Jegatheesan, V. A review of computational fluid dynamics applications in pressure-driven membrane filtration. *Rev. Environ. Sci. Biotechnol.* **2014**, *13*, 183–201. [CrossRef]
16. Berman, A.S. Laminar Flow in Channels with Porous Walls. *J. Appl. Phys.* **1953**, *24*, 1232–1235. [CrossRef]
17. Rezaei, H.; Ashtiani, F.Z.; Fouladitajar, A. Effects of operating parameters on fouling mechanism and membrane flux in cross-flow microfiltration of whey. *Desalination* **2011**, *274*, 262–271. [CrossRef]
18. He, Z.; Miller, D.J.; Kasemset, S.; Paul, D.R.; Freeman, B.D. The effect of permeate flux on membrane fouling during microfiltration of oily water. *J. Membr. Sci.* **2017**, *525*, 25–34. [CrossRef]
19. Almojjly, A.; Johnson, D.; Hilal, N. Investigations of the effect of pore size of ceramic membranes on the pilot-scale removal of oil from oil-water emulsion. *J. Water Process Eng.* **2019**, *31*, 100868. [CrossRef]
20. Darvishzadeh, T.; Priezjev, N.V. Effects of crossflow velocity and transmembrane pressure on microfiltration of oil-in-water emulsions. *J. Membr. Sci.* **2012**, *423–424*, 468–476. [CrossRef]
21. Ahmad, A.L.; Lau, K.K.; Bakar, M.Z.A.; Shukor, S.R.A. Integrated CFD simulation of concentration polarization in narrow membrane channel. *Comput. Chem. Eng.* **2005**, *29*, 2087–2095. [CrossRef]
22. Pak, A.; Mohammadi, T.; Hosseinalipour, S.M.; Allahdini, V. CFD modeling of porous membranes. *Desalination* **2008**, *222*, 482–488. [CrossRef]
23. Lotfiyan, H.; Ashtiani, F.Z.; Fouladitajar, A.; Armand, S.B. Computational fluid dynamics modeling and experimental studies of oil-in-water emulsion microfiltration in a flat sheet membrane using Eulerian approach. *J. Membr. Sci.* **2014**, *472*, 1–9. [CrossRef]
24. Zare, M.; Ashtiani, F.Z.; Fouladitajar, A. CFD modeling and simulation of concentration polarization in microfiltration of oil-water emulsions; Application of an Eulerian multiphase model. *Desalination* **2013**, *324*, 37–47. [CrossRef]
25. Behroozi, A.H.; Kasiri, N.; Mohammadi, T. Multi-phenomenal macroscopic investigation of cross-flow membrane flux in microfiltration of oil-in-water emulsion, experimental & computational. *J. Water Process Eng.* **2019**, *32*, 100962. [CrossRef]
26. Hosseini, M.K.; Liu, L.; Hosseini, P.K.; Lee, K.; Miao, J. Performance evaluation of a pilot-scale membrane filtration system for oily wastewater treatment: CFD modeling and scale-up design. *J. Water Process Eng.* **2023**, *52*, 103570. [CrossRef]
27. Oliveira Neto, G.L.; Oliveira, N.G.N.; Delgado, J.M.P.Q.; Nascimento, L.P.C.; Magalhães, H.L.F.; Oliveira, P.L.d.; Gomez, R.S.; Farias Neto, S.R.; Lima, A.G.B. Hydrodynamic and Performance Evaluation of a Porous Ceramic Membrane Module Used on the Water–Oil Separation Process: An Investigation by CFD. *Membranes* **2021**, *11*, 121. [CrossRef]
28. da Costa Pereira, A.B.; Magalhães, H.L.F.; de Lucena Silva, L.P.; Passos, C.A.; Gomez, R.S.; de Brito Correia, B.R.; de Farias Neto, S.R.; de Lima, A.G.B. Oily Water Treatment by Ceramic Membrane: Modeling and Simulation. *Open J. Fluid Dyn.* **2021**, *11*, 1–19. [CrossRef]
29. Nunes, S.A.; Magalhães, H.L.F.; Gomez, R.S.; Vilela, A.F.; Figueiredo, M.J.; Santos, R.S.; Rolim, F.D.; Souza, R.A.A.; Farias Neto, S.R.d.; Lima, A.G.B. Oily Water Separation Process Using Hydrocyclone of Porous Membrane Wall: A Numerical Investigation. *Membranes* **2021**, *11*, 79. [CrossRef]
30. ANSYS Inc. *Ansys Fluent Theory Guide*; ANSYS Inc.: Canonsburg, PA, USA, 2025.
31. Clift, R.; Grace, J.R.; Weber, M.E. *Bubbles, Drops, and Particles*; Academic Press: New York, NY, USA, 1978. [CrossRef]
32. Crow, C.; Sommerfeld, M.; Tsuji, Y. *Multiphase Flows with Droplets and Particles*, 1st ed.; CRC Press: Boca Raton, FL, USA, 1998.
33. Saffman, P.G. The lift on a small sphere in a slow shear flow. *J. Fluid Mech.* **1965**, *22*, 385–400. [CrossRef]

Disclaimer/Publisher's Note: The statements, opinions and data contained in all publications are solely those of the individual author(s) and contributor(s) and not of MDPI and/or the editor(s). MDPI and/or the editor(s) disclaim responsibility for any injury to people or property resulting from any ideas, methods, instructions or products referred to in the content.